The effects of blade structural model fidelity on wind turbine load analysis and computation time

Ozan Gozcu[1] and David R. Verelst[1]

[1]DTU Wind Energy, Technical University of Denmark (DTU), Frederiksborgvej 399, 4000 Roskilde, Denmark

Correspondence to: Ozan Gozcu(ozgo@dtu.dk)

Abstract. Aero-servo-elastic analyses are required to determine the wind turbine loading for a wide range of load cases as specified in certification standards. The floating reference frame (FRF) formulation can be used to model, with sufficient accuracy, the structural response of long and flexible wind turbine blades. Increasing the number of bodies in the FRF formulation of the blade increases both the fidelity of the structural model as well as the size of the problem. However, the turbine load analysis is a coupled aero-servo-elastic analysis, and computation cost does not only depend on the size of the structural model, but also the aerodynamic solver and the iterations between the solvers. This study presents an investigation of the performance of the different fidelity levels as measured by the computational cost and the turbine response (e.g. blade loads, tip clearance, tower top accelerations). The presented analysis is based on state of the art aeroelastic simulations for normal operation in turbulent inflow load cases as defined in a design standard, and is using two 10 MW reference turbines. The results show that the turbine response quickly approaches the results of the highest fidelity model as the number of bodies increases. The increase in computational costs to account for more bodies can almost entirely be compensated by changing the type of the matrix solver from dense to sparse.

Keywords : Geometric non-linearity, multibody simulation, computation cost, aero-servo-elasticity, flutter, HAWC2

1 Introduction

Modern wind turbine blades are large, slender and flexible composite structures with a complex pre-bended and twisted geometry. Over their operational life blades undergo large deflections and rotations due to external loads (e.g. aerodynamic, inertial and control actuator loads). An aero-servo-elastic code or framework is used to accurately calculate the complex dynamical response of wind turbines with large and flexible blades. This has led to the implementation of geometrically nonlinear structural solvers in wind turbine specific aero-servo-elastic codes. For example, the structural solver BeamDyn (Wang et al., 2017) was implemented in FAST (Jonkman and Buhl Jr, 2005) and it uses the geometrically exact beam theory (Hodges, 1990) based on the Legendre-spectral-finite element method. Another example is a recent release of Bladed (DNV, 2016), that uses a multibody formulation (Shabana, 2013; Cardona and Géradin, 2001) to capture large structural deflections of the modelled structures. BHawC (Rubak and Petersen, 2005), is another non-linear aeroelastic wind turbine simulation code which uses a co-rotational formulation to resolve large deflections accurately.

The effect of large blade deflections on the turbine response has been studied since the early 2000's in MW size turbines. Larsen et al. (2004) performed a turbine analysis with linear and nonlinear structural solvers to investigate the effects of large blade deflections on the turbine performance. The authors concluded that the effective rotor area changes due to large blade deflections, and this alters the blade and turbine loading. In their review paper, Hansen et al. (2006) addressed the importance of nonlinear structural dynamics when large displacements occur for various wind turbines components (e.g blades, floating foundations, mooring lines). Riziotis et al. (2008) compared the blade response of a first and second order beam models with HAWC2 (Larsen and Hansen, 2015) results. The authors concluded that the bending-torsion coupling is the main nonlinear effect for the NREL 5 MW blade (Jonkman et al., 2009), and that a linear beam model under predicts the blade torsional loads. Zierath et al. (2014) compared simulation results using different solvers with measurements of a 2.05 MW prototype wind turbine. The best agreement with measurements was obtained when a multibody dynamic solver was used, since it is able to include nonlinear effects due to large deflections. Manolas et al. (2015) investigated the non-linear geometric effects by a comparison of different beam models of the NREL 5 MW. The authors concluded that the effects of geometric non-linearities are still small for the NREL 5 MW turbine, but they also noted that the linear models are very close to their limit (in terms of accurately predicting the relevant deflections). Therefore, the authors recommended that future more flexible blade designs should be studied with nonlinear structural models. Beardsell et al. (2016) investigated the effects of large deflections on fatigue and extreme loads for four different wind turbines. They observed that the non-linear effects are higher for more flexible blades and they suggested that the NREL 5 MW turbine should no longer be considered as a representative of the latest generation of commercial blade designs in terms of length and flexibility. Jonkman et al. (2017) compared the analysis results of various solvers with measurements of a Siemens 2.3MW turbine. They performed the analysis using BHawC, FAST/BeamDyn and FAST/ElastoDyn. The results show that the nonlinear structural solvers (BHawC and BeamDyn), which can also model curved structures, have good agreement with measurements, while the linear solver (ElastoDyn) shows the largest discrepancy. Large blade deflections also alter the aeroelastic stability of turbines. Kallesøe (2011) showed that the coupling between the blade edgewise and torsional degree of freedom (dof) varies as function of blade deflection shape, and that the edgewise damping can decrease due to large blade deflections. Rezaei et al. (2018) showed that the blade deflections alter the damping and stiffness of the NREL 5 MW wind turbine. The authors observed that the linear models overestimates the flutter speed of the turbine.

Literature shows that large blade deflections are important to consider for a turbine response analysis especially for long and flexible blades. The focus of the existing studies is generally limited to the blade response only, and considering a small selection of load cases. However, what is lacking is a full overview of the turbine response, and a broad selection of load cases when comparing linear and nonlinear blade models without mentioning the additional computational time needed by nonlinear models. The aim of this study is to investigate the performance differences between various nonlinear blade modelling "fidelities" (in terms of number of bodies in a floating reference frame) using HAWC2. The performance of a model here is defined by its computational time and how close the loads are compared to a reference case and which is defined as the case with the highest blade model fidelity. The design load cases for power production under normal turbulence according to the IEC 61400 standard (IEC, 2005) are used for model performance comparisons. The steady turbine response of linear and nonlinear blade models are also compared in terms of power, pitch and deflection. The effect of nonlinear blade modeling on

blade stability/flutter limit is investigated by considering a rotor speed run-away case. Additionally, the computational time of the two available matrix solvers (dense and sparse) in HAWC2, which uses augmented FRF formulation (Shabana, 2010), are compared.

In this study the turbine responses of DTU10MW (Bak et al., 2013) and IEA10MW (Bortolotti et al., 2019) are considered with different structural fidelity levels of the blades for 432 load cases according to DLC 1.2 (Hansen et al., 2015). Deterministic load cases (no turbulence) are also considered to evaluate the turbine steady state response at various wind speeds. The loads at different points on the turbine, controller activity, and turbine performance are compared. Section 2.1 introduces the solver (HAWC2) and geometrically nonlinear structure modelling in the multibody (FRF) formulation. Section 2.2 presents the reference wind turbines, load cases and their models as used for this study. Section 3 includes the calculation methods used when post processing the results, the plots of the computation time, steady case results, DLC 1.2 blade results, DLC 1.2 tower and performance results, stability results, and presents a discussion of the results. The conclusions of this study are given in Section 4.

2 Method and Analysis

Evaluating the aero-servo-elastic response of large and flexible wind turbines using time domain simulations under turbulent inflow conditions requires rigorous analysis. Both the aero-servo-elastic solver and the considered model and load cases are therefore carefully outlined in the following two sections. The applied analysis method presented here is based on a numerical experiment of blades with varying structural model fidelity levels.

2.1 Method

The turbine analyses for the presented work were performed with HAWC2 version 12.6, which is a strongly coupled aero-servo-elastic wind turbine simulation tool. The aerodynamic solver of HAWC2 uses the blade element momentum formulation (Madsen et al., 2012; De Vries, 1979; Wilson and Lissaman, 1974) including effects of dynamic stall, dynamic inflow, wind shear on induction, tip loss, tower shadow and large blade deflections. A PID controller algorithm is used to determine the set point of the pitch bearing angle and generator torque. The servo actuators are modelled as a second order dynamical system with an appropriate given frequency and damping. The structural dynamics of HAWC2 are based on a multibody formulation using an augmented FRF method (Shabana, 2010). Each structural element has two nodes with 6 degrees of freedom (dof) and is modelled as a linear classical isotropic or anisotropic Timoshenko beam (Kim et al., 2013). A body, defined in the FRF formulation, can be composed out of an arbitrary number of elements. Bodies are attached to each other with constraints in any of the six dof (three rotations and three translations). The bodies are deflected linearly but their body reference coordinate system follows the translation and rotation from the last node of the previous body in a continuous structure model.

A general wind turbine structure can be build out of N_e elements and N_b bodies with constraints whereas $N_b \leq N_e$. The constraints allow the user to capture the correct non-linear geometrical response of a collection of bodies in a continuous structure as long as the deflections within one body are small (Pavese et al., 2016). In the limit case where a continuous structure
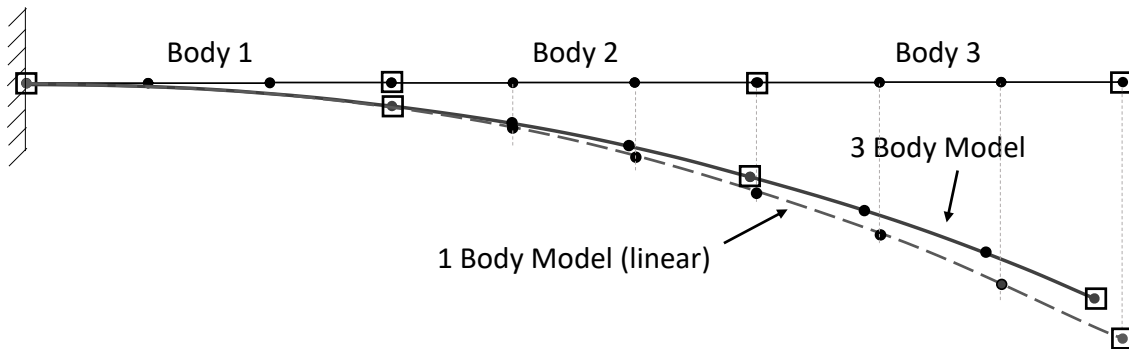
Figure 1. Structural modeling of a cantilever beam in floating reference system with multiple bodies, in deflected and un-deflected states

model has the same number of bodies than elements ($N_b = N_e$), the solution is equivalent to the co-rotational approach (Krenk, 2005; Verelst et al., 2016). For example, Figure 1 shows how the body discretization of a 2D beam structure model captures the nonlinear effect on the beam length as bending deflection occurs. The beam model has nine linear beam elements. The round markers represent the finite element nodes and the square markers represent the body discretization of the structure. As seen in the figure, the one-body model has linear deflections with fictitious elongation due to lack of large rotations, while the three-bodies model shows the large rotation effects due to constraints between the bodies.

HAWC2 constructs a system of differential equations representing the equations of motion of the system with constraints, see equation (1), which is based on a given set of N_e elements and N_b bodies (Shabana, 2013) for i^{th} time step 't_i'. $\boldsymbol{M} \in \mathbb{R}^{N \times N}$, $\boldsymbol{C} \in \mathbb{R}^{N \times N}$, $\boldsymbol{K} \in \mathbb{R}^{N \times N}$ are the inertia, damping and stiffness matrices and N is the number of generalized coordinates. The generalized coordinates, their first and second time derivatives (velocities and accelerations) are shown as $\boldsymbol{u}$, $\dot{\boldsymbol{u}}$ and $\ddot{\boldsymbol{u}}$. Lagrange multipliers and constraint equations are represented by $\boldsymbol{\lambda} \in \mathbb{R}^{N_c}$, $\boldsymbol{g} \in \mathbb{R}^{N_c}$, where N_c is the number of constraints in the model. The Jacobian of constraint equations with respect to the generalized coordinates is presented by $\boldsymbol{G_u} \in \mathbb{R}^{N_c \times N}$. Generalized external forces and quadratic velocity, including gyroscopic and Coriolis force components, vectors are showed as $\boldsymbol{f}$ and $\boldsymbol{f_v}$. The solver computes $\boldsymbol{u}$, $\dot{\boldsymbol{u}}$, $\ddot{\boldsymbol{u}}$ and $\boldsymbol{\lambda}$ at each time step for known external loads while satisfying the constraint equations. In HAWC2, the computed structural response ($\boldsymbol{u}, \dot{\boldsymbol{u}}, \ddot{\boldsymbol{u}}$) is sent to the aerodynamic solver. Based on these state variables, the aerodynamic solver computes the corresponding aerodynamic loads which go into the external force vector ($\boldsymbol{f}$). This load update procedure takes place at each iteration. Hence, the generalized external forces and inertia matrix are a function of time, deflections, velocities and accelerations.

$$\boldsymbol{M}(\boldsymbol{u})\ddot{\boldsymbol{u}}(t_i) + \boldsymbol{C}\dot{\boldsymbol{u}}(t_i) + \boldsymbol{K}\boldsymbol{u}(t_i) + \boldsymbol{G_u}^T(t_i)\boldsymbol{\lambda}(t_i) = \boldsymbol{f}(\boldsymbol{u},\dot{\boldsymbol{u}},t_i) + \boldsymbol{f_v}(\boldsymbol{u},\dot{\boldsymbol{u}},t_i)$$
$$\boldsymbol{g}(t_i) = \boldsymbol{0} \quad , \quad \boldsymbol{G_u}(t_i) = \frac{\partial \boldsymbol{g}(t_i)}{\partial \boldsymbol{u}(t_i)} \tag{1}$$

As the reference/rigid body ($\boldsymbol{u}_r$) and elastic parts ($\boldsymbol{u}_e$) of the generalized coordinates are separated, equation (1) can be written as shown in (2) for body 'j'. The stiffness and damping matrices of the body have only elastic components which are constant for linear elements. Similarly, $\boldsymbol{M}_{ee}$ is also constant and the constant matrices are computed once in a FRF solution

process. The rest of the M matrix needs to be computed at each iteration together with g, G_u, f and f_v since they are state dependent.

$$
\begin{bmatrix} M_{rr}^j & M_{re}^j \\ M_{er}^j & M_{ee}^j \end{bmatrix} \begin{bmatrix} \ddot{u}_r^j \\ \ddot{u}_e^j \end{bmatrix} + \begin{bmatrix} 0 & 0 \\ 0 & C_{ee}^j \end{bmatrix} \begin{bmatrix} \dot{u}_r^j \\ \dot{u}_e^j \end{bmatrix} + \begin{bmatrix} 0 & 0 \\ 0 & K_{ee}^j \end{bmatrix} \begin{bmatrix} u_r^j \\ u_e^j \end{bmatrix} + \begin{bmatrix} G_{u_r}^{jT} \\ G_{u_e}^{jT} \end{bmatrix} \begin{bmatrix} \lambda_r^j \\ \lambda_e^j \end{bmatrix} = \begin{bmatrix} f_{er}^j \\ f_{ee}^j \end{bmatrix} + \begin{bmatrix} f_{vr}^j \\ f_{ve}^j \end{bmatrix} \tag{2}
$$

The main driving factors in computation time of multibody solver are the simulation time, the size of the problem (matrices) and the number of iterations. The vector u_r^j includes six variables to define the position and rotation of the body 'j' reference point. The size of u_e^j depends on the number of element in body 'j'. As more bodies are defined in a model, the number of generalized coordinates and state dependent parts of the matrices increase. For example 1-body example in Figure 1 has 60 generalized coordinates (6 reference coordinates, 54 elastic coordinates), whereas the 3-bodies model has 72 generalized coordinates (18 reference coordinates, 54 elastic coordinates).

In HAWC2 the time integration is performed using the Newmark algorithm (Newmark, 1959) with β and γ constants. The update of the current state was done by $\triangle u$ and $\triangle \lambda$, which are computed according to equation (3). In equation (3) $\triangle r_q$ and $\triangle r_g$ are the force and constraint residuals at current iteration step. K_{eff} is the effective tangent stiffness at the current state, which is shown in equation (4). The sparsity of the constraint Jacobian matrix (G_u) increases with the number of constraints defined in the model. Different numerical approaches can be used when solving dense or sparse matrix problems. HAWC2 can optionally utilize a sparse matrix solution method in which $\triangle \lambda$ from equation (3) is computed using the 'pardiso' sparse matrix routine (Petra et al., 2014a, b). Note that $(G_u K_{eff}^{-1} G_u^T)$ in $\triangle \lambda$ is symmetric and positive definitive for the considered HAWC2 models.

$$
\triangle \lambda = (G_u K_{eff}^{-1} G_u^T)^{-1} (G_u K_{eff}^{-1} \triangle r_q - \triangle r_g)
$$
$$
\triangle u = K_{eff}^{-1} (\triangle r_q - G_u^T \triangle \lambda) \tag{3}
$$

$$
K_{eff} = \frac{1}{\beta h^2} M + \frac{\gamma}{\beta h} C + K \tag{4}
$$

2.2 Analysis

The approach in the study is based on numerical experiments of two turbines: the DTU10MW (Bak et al., 2013) and the IEA10MW (Bortolotti et al., 2019), whose properties are shown in Table 1. It should be noted that the IEA10MW rotor has more prebend, undergoes larger deflections, and exhibits stronger couplings between bending and torsion when compared to the DTU10MW. These three differences are relevant when considering the non-linear geometrical response of a wind turbine rotor.

It is practical to call the bodies used for a continuous structure or a component as main body and the bodies defined in a main body as sub-bodies. A main body can be attached to other bodies or boundaries by constraints in any direction, whereas the constraints between the sub-bodies are always in 6-dof to satisfy the continuity of the structure. In the analyses the number of sub-bodies of the blade varied from 1 (linear response) to 30 (one body for each element, equivalent to a co-rotational approach). The rest of the turbine model was kept the same for a coherent comparison. The HAWC2 models of the considered

Table 1. General properties of the reference wind turbines; DTU10MW and IEA10MW

		DTU10MW	IEA10MW
Blade Length	[m]	86.4	96.2
Hub Radius	[m]	2.8	2.8
Hub Height	[m]	119	119
Shaft Tilt	[deg]	5	6
Rotor Precone	[deg]	2.5	4.0
Rotor Mass	[kg]	41,722	47,742
Nacelle Mass	[kg]	446e5	446e5
Prebend at the Tip	[m]	3.3	6.2
1st Flapwise frequency	[Hz]	0.61	0.42
1st Edgewise frequency	[Hz]	0.93	0.67

turbines for this publication are composed of 9 main bodies: tower, tower top, nacelle, 3 hubs and 3 blades. Table 2 shows the number of sub-bodies in the turbine models and the number of beam elements in each body. The tower, tower top, nacelle and hubs are modelled via 1 sub-body, in other words they are modelled as linear structures. Blades are the only parts which are modelled by multiple sub-bodies to capture large deflections. Both turbine models have 50 aerodynamic sections (or calculation points) on each blade and the open source Basic DTU Wind Energy controller (Hansen and Henriksen, 2013) was used. The turbulence boxes were generated by the Mann turbulence generator (Mann, 1994). A constant time step of 0.01 seconds was used for all considered cases. The computational time was recorded for all cases, and both the sparse and dense matrix solvers were considered.

Table 2. HAWC2 turbine models main bodies, number of elements and sub-bodies used in each main body

Main body name	Number of sub-bodies	Number of elements in main body
Tower	1	10
Tower top	1	1
Nacelle	1	4
Hub	1	1
Blade	1-30	30

The number of bodies in the model alters the problem size since it changes the number of generalized coordinates and constraints in the equations. The generalized coordinates and constraint equations number can be determined by equation (5)-(6). In the equations, N_{mb} is the number of main bodies, and N_{el}^i and N_{sb}^i are the number of elements and sub-bodies in the ith main body. The number of bodies in each blade model varies from 1 to 30. The 30 sub-bodies blade model (similar to

co-rotational model) is the most accurate with the highest N and N_c whereas the 1 sub-body blade case is the linear blade case. Table 2 shows the element numbers at each main body in the turbine models. In all cases, the blades dominate the problem sizes. For example, in the 1-body case the blades have 558 generalized coordinates and 18 constraint equations. For the 30 sub-bodies case, the three blades have 1080 generalized coordinates and 540 constraint equations. Although, the problem size in the FRF formulation changes with the number of bodies defined in the model, the number of independent coordinates $(N - N_c)$ is always 648 for this turbine model.

$$N = \sum_{i=1}^{N_{mb}} (N_{el}^i + N_{sb}^i) \times 6 \tag{5}$$

$$N_c = \sum_{i=1}^{N_{mb}} N_{sb}^i \times 6 \tag{6}$$

Table 3. Number of generalized coordinates N and constraint equations N_c for the full turbine model. The number of sub-bodies refers to the sub-bodies for the different blade models, it does not refer to the total number of sub-bodies of the entire turbine.

Blade sub-bodies	1	2	3	6	9	12	15	18	21	24	27	30
N	702	720	738	792	846	900	954	1008	1062	1116	1170	1224
N_c	54	72	90	144	198	252	306	360	414	468	522	576

The turbine analyses were carried out for steady, deterministic wind load cases, power production load cases according to DLC 1.2 and stability load cases in overspeed conditions. Steady load cases include a full turbine model including controller under a constant wind speed with wind shear and without any yaw error. There are 23 wind speed cases starting from 4 m/s to 26 m/s with a 1 m/s wind step size. Power production load cases according to DLC 1.2 include power production load cases using the normal turbulence model according to the IEC standard. In DLC 1.2 the majority of the fatigue damage of the turbine is procured over its life-time. This can be illustrated by considering the total number of operating hours per DLC and the mean value of the respective 1Hz equivalent loads (see Table 4). Note that the number of operating hours for DLC 1.2 is significantly larger compared to the other cases. Since further the mean 1 Hz equivalent load is either similar or lower, it is safe to assume that DLC 1.2 does indeed drives the life time fatigue load. Consequently, only DLC 1.2 is considered for the current publication. Table 5 summarizes the simulation setup for DLC 1.2 load cases. Note that, according to the IEC standard the use of 6 turbulent seeds is considered sufficient for DLC 1.2. For the analysis here 12 seeds are considered instead in order to increase the robustness of the obtained fatigue damage (Tibaldi et al., 2014) for each number of sub-bodies case. In general terms further attention should be paid when comparing results from turbulent time domain simulations of nearly identical turbine models. Extreme loads can vary significantly when a large rotor is positioned slightly different with respect to a specific temporal turbulent structure in the wind field (Natarajan and Verelst, 2012). For this analysis it can cause, potentially, large extreme load variations between the simulations of the same wind speed and seed number, but different number of sub-bodies. Such differences could be driven not by the difference in modelling (1 to 30 sub-bodies for this investigation), but by small differences in rotor azimuthal position at a specific time at which an extreme event occurs.

Table 4. Qualitative breakdown of the fatigue load contributions of various design load cases for the IEA10MW (based on the loads reported in (Bortolotti et al., 2019)). Hour distribution is based on a 20-year lifetime.

DLC	hours	mean blade root flapwise 1Hz DEL (m=10)
DLC 1.2	158605	21787 kNm
DLC 2.4	927	21868 kNm
DLC 3.1	1528	20163 kNm
DLC 4.1	1528	17782 kNm
DLC 6.4	4081	13482 kNm

Table 5. Design load cases (DLC) 1.2 power production on normal turbulence load case simulation setup

Simulation setup	Length: 600 s
	Wind: 4 - 26 m/s with steps of 2 m/s
	Yaw: -10/0/+10 deg
	Turbulence: 12 seeds per wind speed and yaw error
	Shear: Vertical and exponent of 0.2
	Gust: None
	Fault: None
Total no. simulations	432

The stability analysis includes a turbine model which is free to speed up without generator torque and has a fixed blade pitch angle at zero degree (Pirrung et al., 2014). A steady state rotor speed under zero aerodynamic torque is found close the cut-in wind speed. From there, the wind speed is increased following a shallow linear ramp. Consequently, the rotor slowly accelerates. The instability is than determined when significant blade vibrations are observed.

3 Results

The results of the blade models with different number of sub-bodies are compared to the blade with the 30 bodies case (highest fidelity). The loads and total number of iterations are normalized with respect to the highest fidelity results, while the computation time is normalized with respect to the lowest fidelity model (1 sub-body/linear case) in combination with the dense matrix solver. The computation time and total iteration number are defined here as the total central processing unit (CPU) time and the sum of iterations for all load cases, respectively.

The activity of the pitch bearing is evaluated by integrating the pitch angle signal over time for all load cases and summed up into ϕ_{total}, see equation (7). The pitch angular speed of jth blade at i^{th} time step is shown by $\dot{\phi}_i^j$. There are N_t number of time steps in all load cases. In addition to the total pitch angle change ϕ_{total}, the power needed by the pitch actuator (P_i^j) of
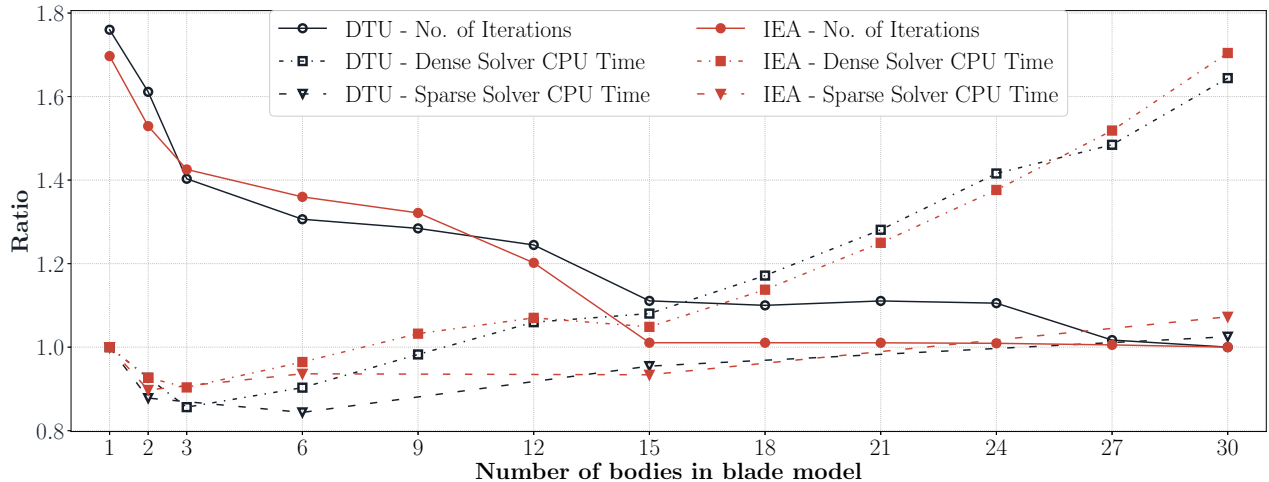
Figure 2. The total number of iterations is normalized by the result of the 30 sub-bodies case, and the total CPU time is normalized by the 1 sub-body dense matrix solver case for the DTU and IEA turbines. The CPU time ratios are given for both dense and sparse solvers.

j^{th} blade at i^{th} time step is calculated by considering the torsion moment at the blade root (M_i^j) and angular speed of the pitch bearing $\dot{\phi}_i^j$, see Equation (8). Note that the bearing friction is neglected in the equation. The max power needed by the pitch actuator might determine the size of the component (i.e. actuator, bearing etc.).

$$\phi_{total} = \sum_{j=1}^{3}\sum_{i=1}^{N_t} \frac{\dot{\phi}_{i-1}^j + \dot{\phi}_i^j}{2}\Delta t_i \tag{7}$$

$$P_i^j = M_i^j \times \dot{\phi}_i^j \quad \text{at } i^{th} \text{ time step} \tag{8}$$

Figure 2 shows DLC 1.2 load cases computation time and number of total iteration ratios of both turbines for dense and sparse matrix solvers. The computation time ratio is calculated with respect to the linear (1 sub-body) case using the dense solver, and number of iterations ratio is calculated with respect to the 30 sub-bodies blade case, which has the lowest number of iterations for both turbine models. The total number of iterations does not change for sparse and dense matrix solver types, therefore there is only one curve for the number of iterations. The dense matrix solver CPU time results are given only for 1, 2, 6, 15 and 30 sub-bodies cases. The computation time is dependent on the number of iterations observed in a simulation and the number of sub-bodies of the blade. Therefore, it is possible to observe a decrease in computation time as the number of dofs and constraint equations increases. The number of iterations decreases until the 15 sub-bodies case, which also affects the CPU time accordingly. After 15 sub-bodies case, the number of iterations remains approximately constant and correspondingly, the CPU time increases as the number of bodies increases.

The maximum dense solver computation time is observed for the 30 sub-bodies case. It is is approximately 62% and 70% (see Figure 2) slower compared to the linear case for the DTU10MW and IEA10MW. Due to a sharp reduction in the number of iterations between the 1 - 3 sub-body cases the computational time decreases as well even though the complexity of the model

increases. Hence, the dense solver computational cost due to the increase of model complexity raises slower compared to the time gained by having less iterations. The number of iterations decreases only moderately between 3-15 sub-bodies cases, and which is followed by a modest increase in computational time. It is only after the 15 sub-bodies cases, for which the total number of iterations is roughly constant, a continuous increase of the computational time is observed as function of number of sub-bodies. It is further interesting to note that there is no significant difference in terms of computational cost between the 1 and 15 sub-bodies cases due to the fact that approximately 36% and 41% fewer iterations were observed for the DTU10MW and IEA10MW respectively.

Since the sparsity of the matrices in the solution process increases with the number of bodies, sparse matrix solver becomes computationally more efficient for models with many constraints or bodies (Dibold et al., 2007). Although not shown here, no difference was observed between the results of the dense and sparse matrix solvers. For the linear case, the CPU time is almost the same for both solver types. The sparse solver is significantly faster for the non-linear (multibody) cases. The computational speed up for the 15 sub-bodies case is about 11% and it is actually faster than the linear case with dense matrix solver. Obtaining the sparse solution of 30 sub-bodies cases for IEA turbine is about 36% faster than the using dense matrix techniques. The highest fidelity model with sparse matrix solver is just 9% slower than the linear case for IEA turbine and this number goes down to 4% for DTU turbine.

3.1 Steady Wind Case Results

Turbine power, blade pitch, blade effective radius change and blade tip torsion results are given for steady, deterministic wind speed conditions. Figure 3 shows the power, pitch and blade effective radius change results of linear (1 body) and nonlinear (30 body) blade models for steady wind load cases. The DTU10MW results are shown on the left, while the IEA10MW results are shown on the right. The difference between linear and nonlinear blade models are smaller for the DTU turbine than the IEA turbine. Power differences are observed only at the below rated wind speeds whereas the pitch angles are different at the above rated wind speeds. Blade effective radius shows the blade projected to the rotation plane. Blade effective radius change differences between linear and nonlinear models are the main reasons of the pitch and power differences. Power difference reaches up to 0.3 MW at 10 m/s wind speed where the blade radius difference is around 3 meters for IEA turbine. Since the linear blade model gives longer blade effective radius, the computed turbine power is higher for the linear blade model. However, this difference doesn't affect the annual energy production (AEP) significantly, because the power difference is small and it occurs only at the below rated wind speeds where the power is already low. The AEP difference is less than 1 %, which is consistent with DLC 1.2 results mentioned in Section 3.3. The pitch angle difference between linear and nonlinear models reaches up to 0.24 degrees at 11 m/s for IEA turbine when the nonlinear blade model pitch is 2.79 degrees.

Figure 4 shows blade torsion deformations results at 75% blade span and blade tip for linear and nonlinear blade models. Since the IEA blade is more flexible and longer than DTU blade, the IEA torsional deflections are up to 1 degree larger than DTU deflections. The blade torsion deflections are large enough (up to 2.4 degrees at IEA blade tip) to alter the turbine loads and performance. The deflections become significant especially after the rated wind speed where the pitch activity is high.
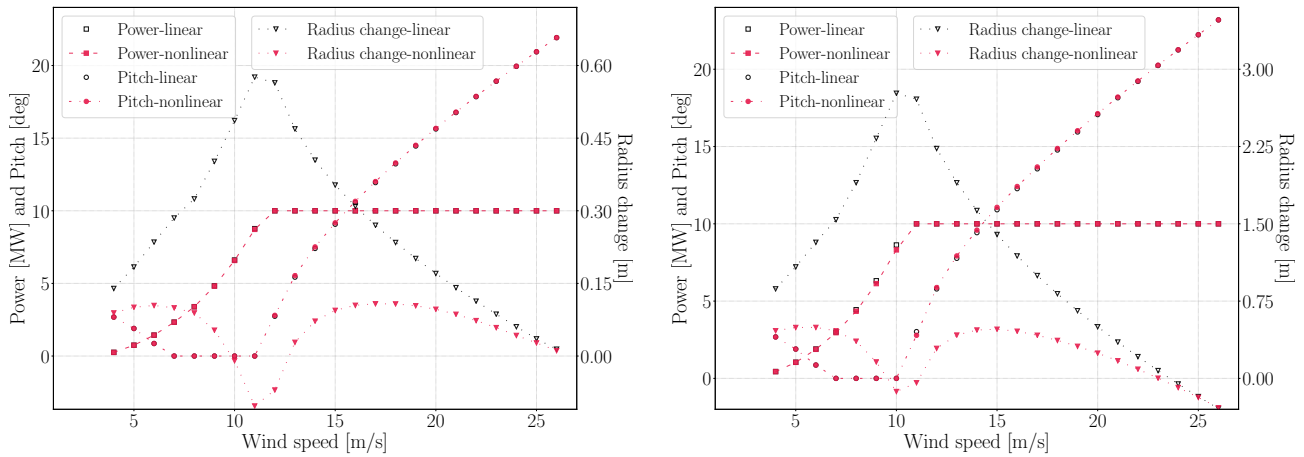
Figure 3. Linear and nonlinear blade model power, blade pitch (left axis in the figures) and effective blade radius change (right axis in the figures) results with respect to wind speeds for steady wind load cases. The left figure shows the DTU10MW results and IEA results are given in the right figure.

Although, the torsional deformation curves with respect to wind speeds are similar for DTU blade models, IEA blade model deformation curves look different after the rated wind speed.
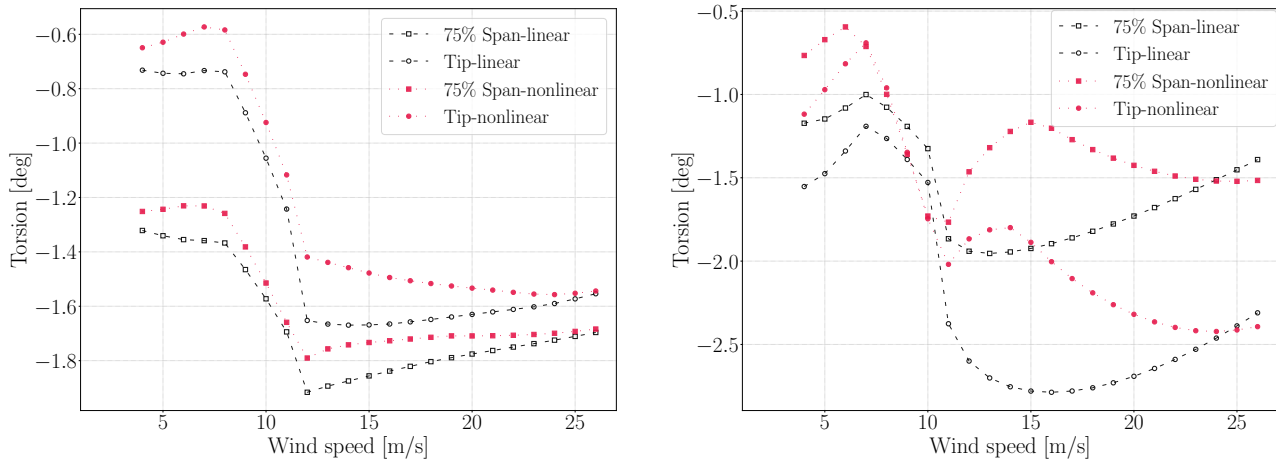
Figure 4. Linear and nonlinear blade model torsion deformations at 75% blade span and blade tip with respect to wind speeds for steady wind load cases. The left figure shows the DTU10MW results and IEA results are given in the right figure.

3.2 DLC 1.2 Blade Results

Turbine blade deflection, damage equivalent load, maximum load and cross-section load results are given for DLC 1.2 load cases. Figure 5 shows the normalized minimum blade tip-tower clearance, maximum effective blade radius (blade tip axial

position according to blade root coordinate system) and maximum edgewise deflections. The minimum tower clearance is an important design criteria and it mostly depends on the flapwise deflection of the blades. The linear case computes lower tower clearance (larger blade deflections) than non-linear models and a nice approaching trend to the highest fidelity results is observed with increasing number of bodies. After 15 sub-bodies the deviation from the 30 sub-bodies case becomes negligible.

5 The maximum difference reaches about 5 meters, which means 80% deviation from the highest fidelity case for the more flexible IEA turbine. There is a faster approach to the highest fidelity results in the effective blade radius plot than the tower clearance. The IEA turbine has again a larger difference between the linear and nonlinear blade models. The diameter difference can reach up to 7 meters for the IEA rotor and 1.7 meters for the DTU rotor. The linear model consequently has a longer blade length than the non-linear models due to the prebend in the blade design. The elastic part of inertia and stiffness matrices in

10 the linear case do not change as function of blade deflection. In other words, the linear model does not update the couplings between the various different dofs as the blades deforms. The undeformed blade has a flapwise - axial displacement coupling in which the positive flapwise displacements (in the flow direction) cause an increase in blade length according to the blade root coordinate system. However, this coupling changes the sign after a certain point for the nonlinear models. The edgewise deflections computed by the linear model differs up to 10% compared to the nonlinear case.
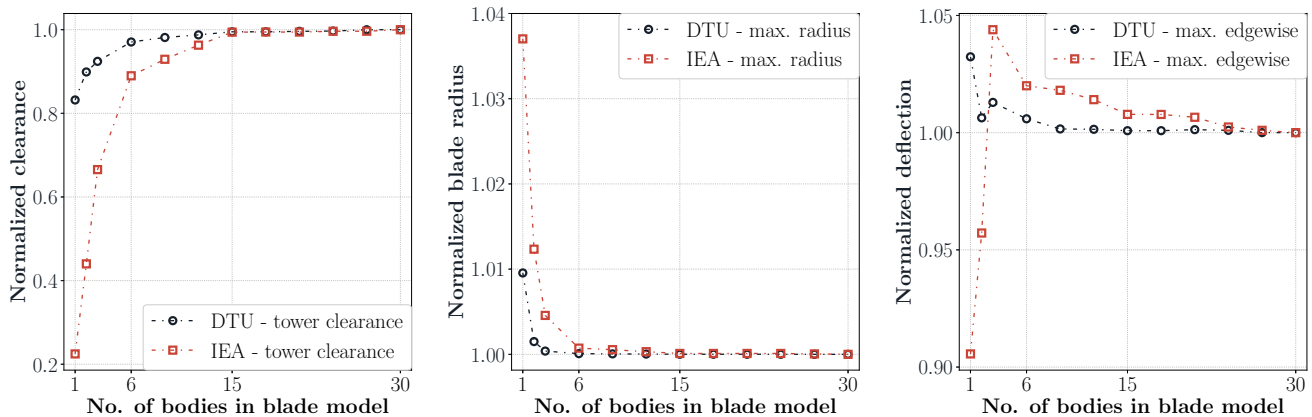
Figure 5. Normalized blade tip minimum tower clearance, maximum effective blade radius and blade edgewise deflection results. Values are normalized with respect to the results of the 30 sub-bodies case.

15 Figure 6 shows the life time damage equivalent load (DEL) ratios between the linear (1 sub-body) and nonlinear (30 sub-bodies) blade models over the normalized blade span for the DTU10MW and the IEA10MW turbines. The IEA turbine has a larger difference between linear and nonlinear cases in edgewise and flapwise DEL moment than the DTU turbine, but not so for the torsion DEL. A significant difference between the linear and nonlinear case (30 sub-bodies) of more than 20% can be observed for certain outboard radial stations. The flap- and edgewise DELs are consistently overestimated for the linear case,

20 while the torsion DEL is underestimated with respect to the 30 sub-bodies nonlinear case.

Figure 7 shows flapwise, edgewise and torsion moment DEL ratio variations by model fidelity (number of sub-bodies in blade model) at blade stations where the maximum deviations between linear and non-linear cases occur for each load component.
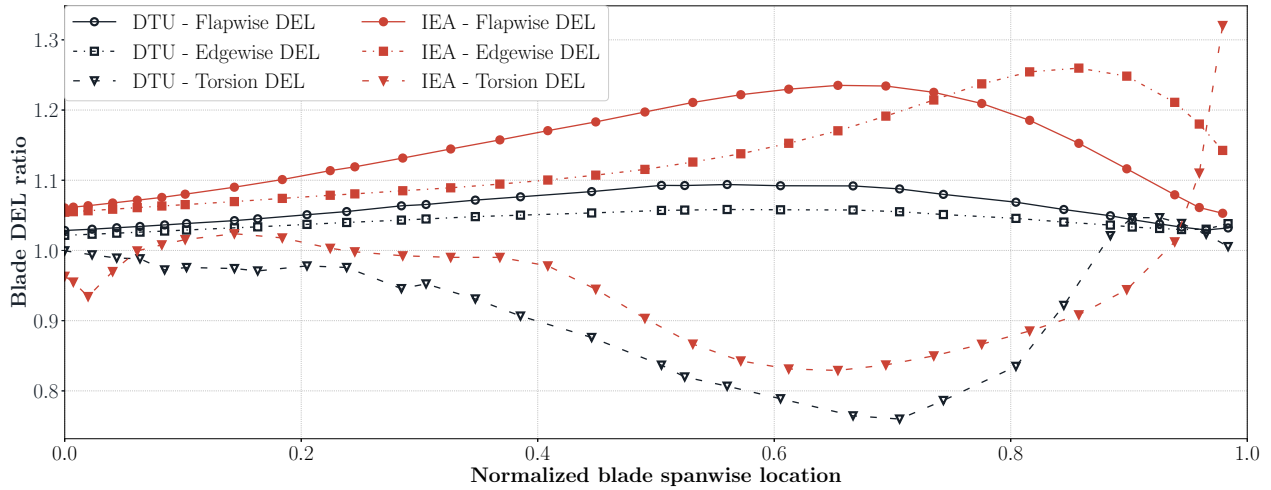
Figure 6. Flapwise, edgewise and torsion moment DEL ratios between linear (1 sub-body) and nonlinear (30 sub-bodies) blade model over the normalized blade span for DTU10MW and IEA10MW turbines.
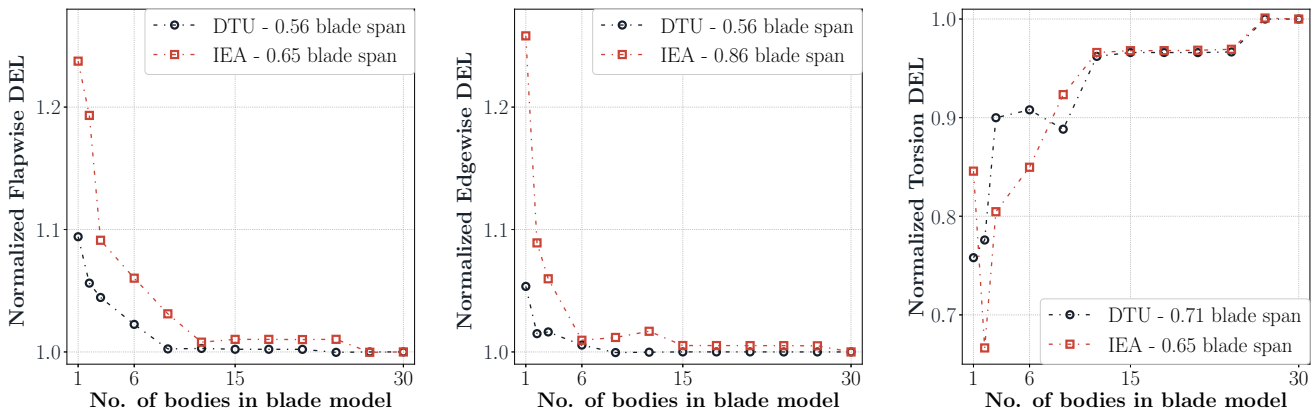
Figure 7. Normalized flapwise, edgewise and torsion moment DEL ratio variations with respect to the number of blade model sub-bodies at blade stations where the maximum deviations between linear and non-linear cases occur

The results are normalized with respect to the highest fidelity blade model. The maximum deviation of the IEA turbine in flapwise deviation is 24% and it raises to 26% in edgewise direction. The DTU turbine has 9% and 5% deviations in flapwise and edgewise directions. The results of both turbines in flapwise and edgewise directions have a similar trend meaning that after 15 sub-bodies the deviations become very small. The torsion DEL has the largest deviations for both turbines, and only after the 9 sub-bodies case a consistent reduction in difference between the linear and nonlinear case can be observed. The deviations become quite small for cases with 27 sub-bodies or more.
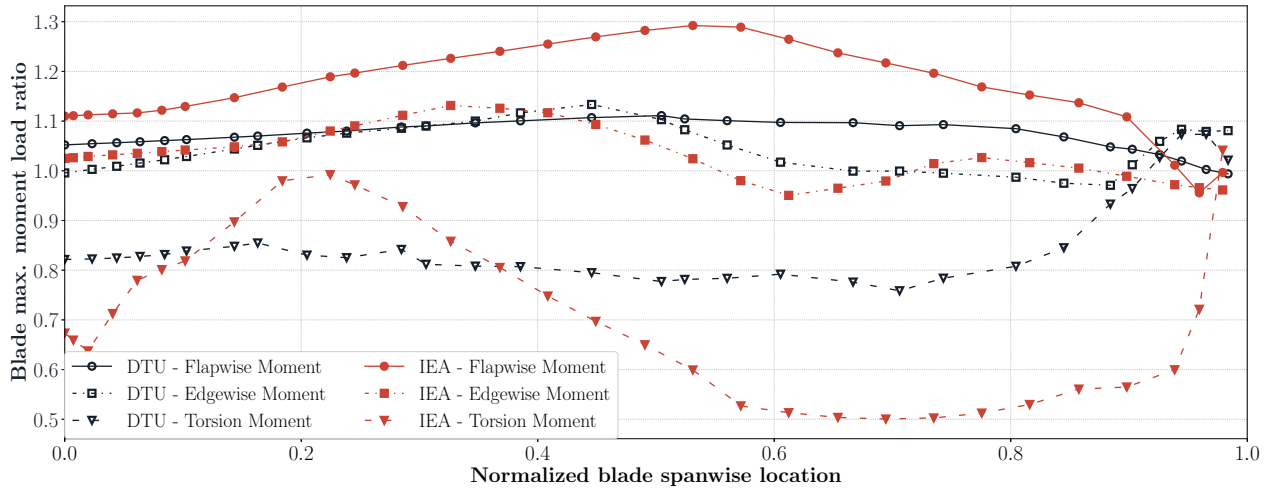
Figure 8. Linear and nonlinear blade absolute maximum moment load result ratio variation of DTU10MW and IEA10MW turbines with respect to blade span location

Figure 8 shows the absolute maximum moment load result ratio between linear and nonlinear blade models over the normalized blade spanwise locations. The IEA results have generally larger deviations than the DTU results. The largest difference occurs in torsion moments for both turbines. The difference in flapwise direction reaches up to 30% for the IEA turbine and 10% for the DTU turbine. The edgewise deviations of both turbines reach up to 12%. The torsion moment deviation hits 50% in some blade regions for the IEA turbine. The torsion moments are underestimated by linear models whereas the flapwise and edgewise moments are generally overestimated by linear models.

Alternatively, the ultimate cross sectional loads can visualized by considering the load envelopes. The load envelopes are the concave boundaries of the flap- and edgewise bending moment time traces considering all load cases. In doing so, the absolute magnitude and corresponding angle of the extreme loads are visualized. Figure 9 shows the cross-section flapwise and edgewise moments envelopes at blade stations where the largest deviations between linear and nonlinear cases are observed for the maximum flapwise moment load (as can be determined from Figure 8). The largest flapwise moment deviation occurs at 43.6 and 51.1 meters blade radius for the DTU and the IEA turbines. Figure 9 shows the load envelopes for 1, 2, 6, 15 and 30 sub-bodies cases. The linear model is generally conservative with respect to the nonlinear models, and the DTU turbine has smaller difference between linear and nonlinear blade models compared to the IEA turbine.

3.3 DLC 1.2 Tower and Performance Results

Turbine tower damage equivalent load, maximum and cross-section load results are given for DLC 1.2 load cases. The turbine performance results are also mentioned here. Figure 10 shows the normalized maximum tower top (yaw bearing) torsion moments and maximum tower top accelerations. In case of excessive tower top accelerations, the controller starts an emergency
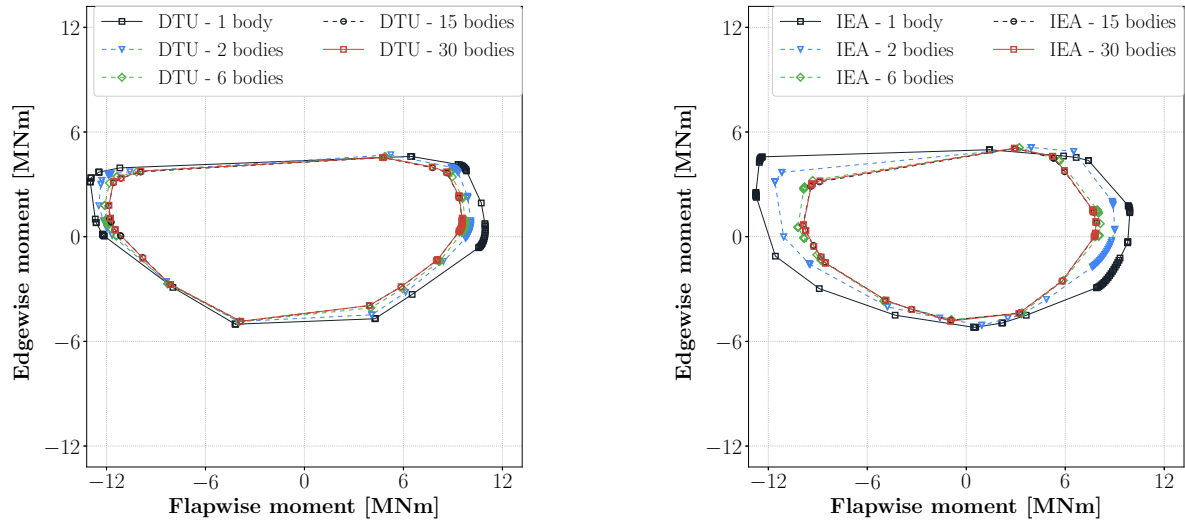
Figure 9. Cross section flapwise and edgewise load envelopes at 43.6 meters blade radius of the DTU turbine, and 51.1 meters blade radius of the IEA turbine for 1, 2, 6, 15 and 30 sub-bodies cases

stop procedure. The difference in yaw bearing torsion moment can reach up to 10% for the IEA turbine. The results approach to the highest fidelity results very fast, and after the 9 sub-bodies case the deviations become very small compared to the 30 sub-bodies cases. The difference in tower top accelerations can be more than 4% between the linear and nonlinear case.
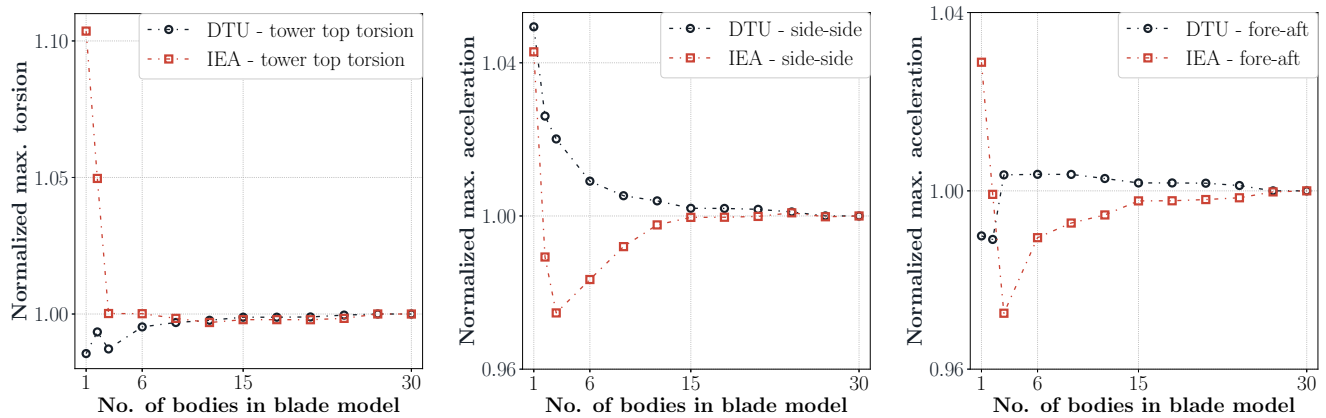
Figure 10. Normalized tower top maximum torsion moments, side-side and fore-aft accelerations. Values are normalized with respect to the the results of the 30 sub-bodies case.

Figure 11 shows the DELs of the fore-aft (moment force vector perpendicular to wind direction) and side-side (moment force vector aligned with the wind direction) moments at the tower top position where the yaw actuator and bearings are located. There is a negligible deviation between the linear and nonlinear case for the side-side DEL moments for both turbine models. However, the deviations in fore-aft and torsion DELs exceed 4% for the IEA turbine and reach to 3% for the DTU turbine. The

results approach the highest fidelity model results smoothly and the deviation becomes very small after 15 sub-bodies cases for all channels. Figure 12 shows the tower bottom side-side and fore-aft moment load envelopes of the turbines for 1, 2, 6, 15 and 30 sub-bodies cases. The deviations between linear and non-linear cases are more explicit in the IEA10MW turbine than the DTU10MW turbine. In contrast to the blade moment envelopes, the linear case is not always the more conservative approach compared to the nonlinear cases.
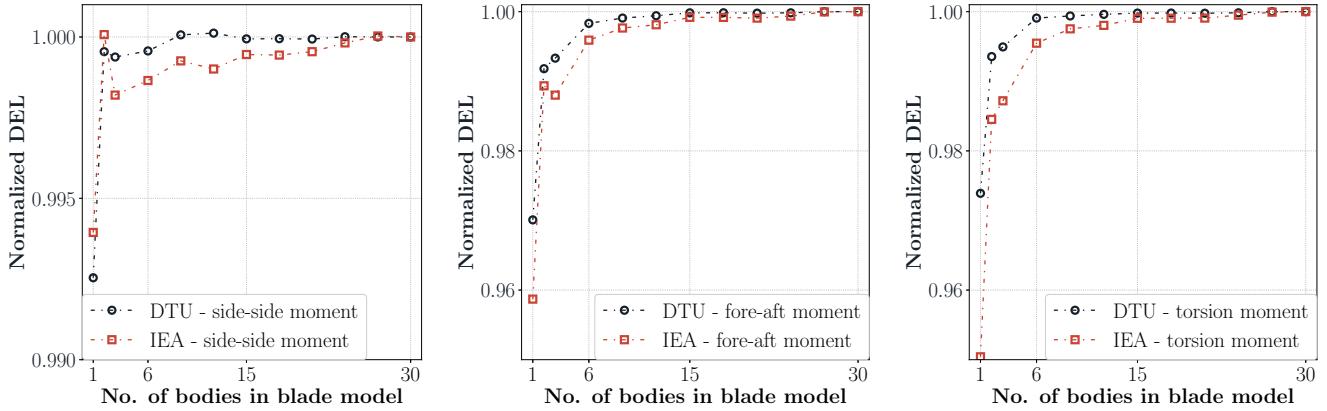
Figure 11. Normalized tower top side-side, fore-aft and torsion DEL moment with respect to number of sub-bodies in blade model
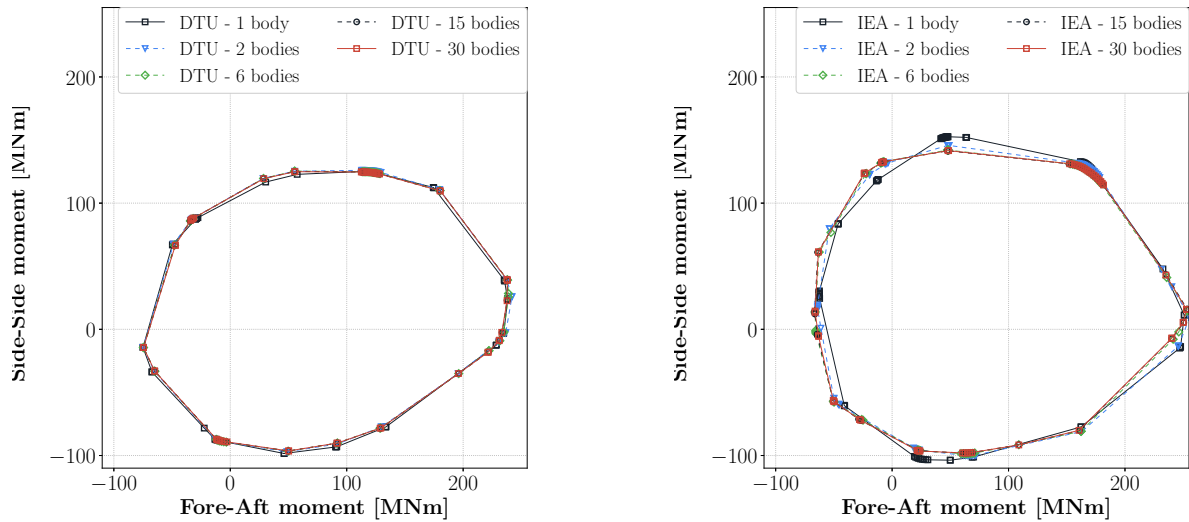
Figure 12. Tower bottom fore-aft and side-side load envelopes of the DTU and the IEA turbines for 1, 2, 6, 15 and 30 sub-bodies cases

Figure 13 shows the normalized blade pitch actuator DEL, total pitch angle change of the turbines in all simulations computed by equation (7), and maximum power at pitch actuator computed via the equation (8). The IEA turbine has a deviation of about 3% in cumulative pitch angle results. This indicates that the controller activity is also affected by the fidelity of blade modelling. The maximum pitch actuator power depends on both blade root torsion moment and pitch angle speed. A very

large deviation is observed in the pitch power results, which are 38% and 34% for the DTU and IEA turbines respectively. The deviations in the IEA turbine results are generally higher than the DTU10MW turbine results, however the DTU turbine has larger deviations in terms of percentage than the IEA turbine in pitch power results. Although the highest fidelity model causes slightly less pitch activity compared to the linear model, the actuator power increases significantly with the fidelity of the blade model. This is due to significantly increased blade torsional moments with increasing blade model fidelity.
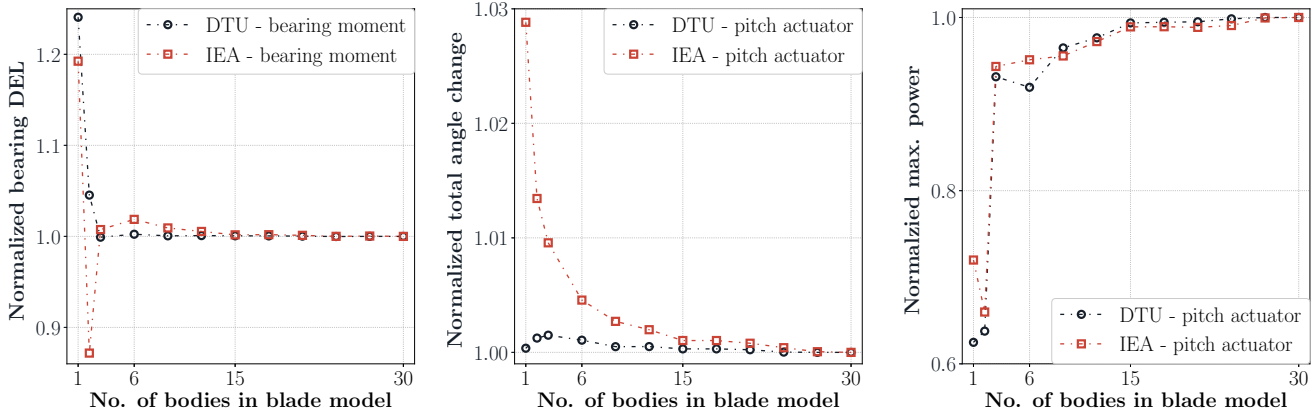
Figure 13. Normalized blade pitch actuator (blade root torsion moment) DEL, total pitch angle change for all load cases, and maximum power at pitch actuator with respect to number of blade sub-bodies

The annual energy production (AEP) for the different blade models is well below 1.0%. This difference is relatively small when compared to the loads since the controller tracks the optimal operating conditions below rated wind speed, and maintains the rated power above rated wind speed. Consequently, only in below rated conditions a very small difference in power output can be observed whereby the linear case results in small increase in power output compared to the nonlinear 30-sub body case.

3.4 Stability Results

The stability of DTU and IEA turbines are evaluated by considering the linear (1 body) and nonlinear (30 body) blade models. Blade tip torsion deformation depicts the blade vibrations and instability (flutter) clearly. Figure 14 shows the rotor speed and blade tip torsion results with respect to wind speed. Turbines have zero aerodynamic torque at the initial wind speed and wind speed acceleration is $0.0145 \ m/s^2$. Results shows that DTU turbine has much higher flutter speeds than IEA turbine for both blade models. The DTU linear blade model (blue curve) flutter speed occurs at a 1 m/s higher wind speed compared to the nonlinear model (red curve). However, for the IEA linear model, flutter occurs at a wind speed which is 3.6 m/s lower compared to the nonlinear model. This shows that the linear models do not always overestimates the flutter speeds and is actually model dependent.
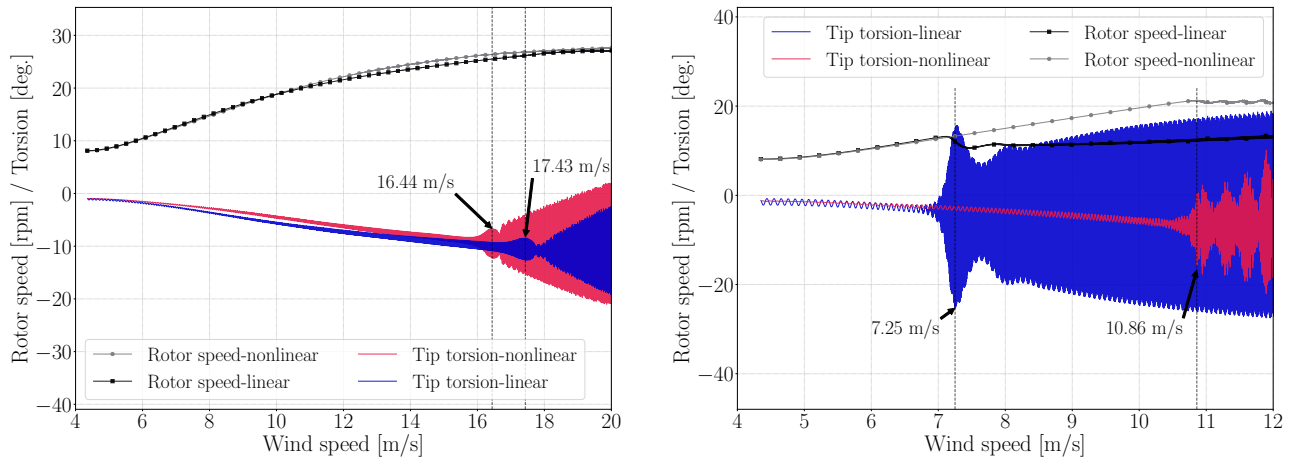
Figure 14. DTU10MW (left figure) and IEA (right figure) rotor speed and blade tip torsion deformation results with respect to wind speed. The flutter wind speeds are shown in the figures.

4 Discussion and Conclusion

The effects of blade structural model fidelity on the turbine response, loads, stability and computation time are investigated in this study. The blades are modelled by different number of sub-bodies in the multibody formulation of HAWC2. The blade model geometric non-linearity is changed from linear to the highest available fidelity level, which is equivalent to a co-rotational

5 formulation. The effects of blade geometric non-linearities are compared by exploring the results of two different blade designs with otherwise identical tower and shaft configuration. The normal power production load cases are selected according to the IEC 61400-1 standard (DLC1.2), but considering 12 instead of 6 turbulent seeds. In addition, the computational speed of the dense and sparse matrix solvers as used by HAWC2 are compared for different blade model fidelities.

CPU time can decrease by increasing the number of bodies, since the total number of aero-elastic iterations decreases as the

10 number of bodies increases. After the total number of aero-elastic iterations becomes independent of the number of bodies, the CPU time increases by the number of bodies explicitly. The linear models have larger deflections compared to the non-linear models and these large deflections cause larger changes in the aerodynamic forces. Consequently, the cycle between the structural response and aerodynamic forces requires more iterations for linear models. Since the sparsity of the matrices increases by the number of bodies, the sparse solver becomes more effective than the dense solver in terms of required CPU

15 time for nonlinear problems. The geometric nonlinear effects are the most apparent in the blade responses. The effective blade length, computed by linear and nonlinear blade models is different up to 3 meters for steady load cases. Hence, they have different turbine power at below rated wind speeds and different pitch at above rated wind speeds. A significant difference in blade tip-tower clearance is observed of up to 5 meters, while the maximum blade tip radius can be close to 4% higher when comparing the linear to the 30 sub-bodies model for DLC 1.2 load cases. The most significant differences are noted for mid- and

20 outboard blade sections and their maximum and DEL bending moments. Depending on the blade model, the linear 1 sub-body

model overestimates flap- and edgewise DELs up to 30%, while the torsional DEL moments are underestimated up to 25%. A similar trend is shown for the maximum loads: an overestimate of up to 30% for the flap-wise extreme bending moment, and an underestimated maximum torsional moment of almost 50% when comparing the 1 and 30 sub-bodies cases. The tower loads, however, are much less dependent on the number of blade sub-bodies. For the tower top the largest noted differences are around 4% for the yawing moment, but with one important distinction that fewer sub-bodies consistently underestimate rather than overestimate the loading. Further investigation is needed to understand the physical reason behind the yaw moment difference between linear and nonlinear models. The tower bottom loads are virtually unaffected as function of blade sub-bodies. The pitch actuator maximum power is significantly underestimated up to 30-40% by the 1 sub-body blade compared to 30. The performance parameters such as power, AEP, rotational speed, thrust and shaft moment remained virtually unaffected by blade model fidelity for both steady wind and DLC 1.2 cases. Finally, the flutter speed can be different more than 3 m/s for linear and nonlinear blade models and linear model is not always overestimates the flutter speed.

Although there are significant differences between the linear and non-linear blade model (with 30 sub-bodies), the results generally approach the highest fidelity results fast as the number of blade sub-bodies increases. In most cases the deviations in results become insignificant after 15 sub-bodies. This is also the point after which the total number of iterations does not reduce any further significantly with increasing number of sub-bodies.

The work outlined here confirms earlier studies that the nonlinear geometrical effects are significant for wind turbine blades, and that this importance is related to the size, prebend shape, and flexibility of the considered blade model. The authors conclude that users are recommended to model blades with as many sub-bodies as there are structural elements, while also using a sparse matrix solver for models that have symmetric effective stiffness matrices in HAWC2. In doing so within the context of HAWC2, no increase in CPU time is noted while at the same time having the blade model with the highest structural fidelity.

Author contributions. OG conducted the study as part of his PhD research. The idea was developed by OG and DRV. OG ran the analyses and did the post-processing including results and figures by tools developed DRV. Manuscript was written jointly by OG and DRV.

Competing interests. DTU Wind Energy develops, supports, and distributes HAWC2 on commercial terms.

Acknowledgements. The study was funded by Ozan Gozcu's PhD project and HAWC2 Development project in DTU Wind Energy. Authors are grateful to Sergio González Horcas and Anders Melchior Hansen for their contribution to HAWC2 solver. Furthermore, authors would like to acknowledge their colleagues, Sergio González Horcas, Mathias Stolpe, Suguang Dou, Riccardo Riva and Georg Pirrung for their comments to the manuscript.

References

BLADED 4.8 Theory Manual, DNV GL, 2016.

Bak, C., Zahle, F., Bitsche, R., Kim, T., Yde, A., Henriksen, L. C., Hansen, M. H., and Natarajan, A.: The DTU 10-MW Reference Wind Turbine, Tech. Rep. Report-I-0092, DTU Wind Energy, 2013.

5 Beardsell, A., Collier, W., and Han, T.: Effect of linear and non-linear blade modelling techniques on simulated fatigue and extreme loads using Bladed, Journal of Physics: Conference Series, 753, 2016.

Bortolotti, P., Canet Tarrés, H., Dykes, K., Merz, K., Sethuraman, L., Verelst, D., and Zahle, F.: IEA Wind Task 37 on System Engineering in Wind Energy WP2.1 Reference Wind Turbines, To be published, 2019.

Cardona, A. and Géradin, M.: Flexible multibody dynamics: a finite element approach, John Wiley, 2001.

10 De Vries, O.: Fluid dynamic aspects of wind energy conversion, Advisory Group for Aerospace Research and Development Neuilly-Sur-Seine, AGARD-AG-243, 1979.

Dibold, M., Gerstmayr, J., and Irschik, H.: On the accuracy and computational costs of the absolute nodal coordinate and the floating frame of reference formulation in deformable multibody systems, ASME International Design Engineering Technical Conferences, pp. 1071–1080, 2007.

15 Hansen, M. H. and Henriksen, L. C.: Basic DTU Wind Energy Controller, DTU Wind Energy, No. 0028, 2013.

Hansen, M. H., Thomsen, K., Natarajan, A., and Barlas, A.: Design Load Basis for Onshore Turbines, DTU Wind Energy, No. 0174, 2015.

Hansen, M. O. L., Sørensen, J. N., Voutsinas, S., Sørensen, N., and Madsen, H. A.: State of the Art in Wind Turbine Aerodynamics and Aeroelasticity, Progress in aerospace sciences, 42, 285–330, 2006.

Hodges, D. H.: A mixed variational formulation based on exact intrinsic equations for dynamics of moving beams, International Journal of

20 Solids and Structures, 26, 1253–1273, 1990.

IEC: 2005 IEC 61400-1 3rd edition Wind turbines - Part 1: Design requirements, International Electrotechnical Commission,IEC, 2005.

Jonkman, J., Butterfield, S., Musial, W., and Scott, G.: Definition of a 5-MW Reference Wind Turbine for Offshore System Development, National Renewable Energy Laboratory, Technical Report No. NREL/TP-500-38060, 2009.

Jonkman, J., Sprague, M. A., Shreck, S., Wang, Q., Guntur, S. K., and Sievers, R.: A validation and code-to-code verification of FAST for a

25 megawatt-scale wind turbine with aeroelastically tailored blades, Wind Energy Science, 2, 2017.

Jonkman, J. M. and Buhl Jr, M. L.: FAST User's Guide, National Renewable Energy Laboratory (NREL), 2005.

Kallesøe, B. S.: Effect of steady deflections on the aeroelastic stability of a turbine blade, Wind Energy, 14, 209–224, https://doi.org/10.1002/we.413, 2011.

Kim, T., Hansen, A. M., and Branner, K.: Development of an anisotropic beam finite element for composite wind turbine blades in multibody

30 system, Renewable Energy, 59, 172–183, 2013.

Krenk, S.: Nonlinear Modelling and Analysis of Structures and Solids, Cambridge University Press, 2005.

Larsen, T. J. and Hansen, A. M.: How 2 HAWC2 the user's manual, Risø-R-1597(ver. 4-6)(EN), 2015.

Larsen, T. J., Hansen, A. M., and Buhl, T.: Aeroelastic effects of large blade deflections for wind turbines, Special topic conference: The science of making torque from wind, pp. 238–246, 2004.

35 Madsen, H. A., Riziotis, V., Zahle, F., Hansen, M. O. L., Snel, H., Grasso, F., Larsen, T. J., Politis, E., and Rasmussen, F.: Blade element momentum modeling of inflow with shear in comparison with advanced model results, Wind Energy, 15, 63–81, 2012.

Mann, J.: The spatial structure of neutral atmospheric surface-layer turbulence, Journal of fluid mechanics, 273, 141–168, 1994.

Manolas, D., Riziotis, V., and Voutsinas, S.: Assessing the importance of geometric nonlinear effects in the prediction of wind turbine blade loads, Journal of Computational and Nonlinear Dynamics, 10, 2015.

Natarajan, A. and Verelst, D. R.: Outlier robustness for wind turbine extrapolated extreme loads, Wind Energy, 15, 679–697, https://doi.org/10.1002/we.497, 2012.

5   Newmark, N. M.: A method of computation for structural dynamics, Journal of the Engineering Mechanics Division, 85, 67–94, 1959.

Pavese, C., Kim, T., Wang, Q., Jonkman, J., and Sprague, M. A.: Hawc2 and beamdyn: Comparison between beam structural models for aero-servo-elastic frameworks, National Renewable Energy Lab.(NREL) Technical Report, 2016.

Petra, C. G., Schenk, O., and Anitescu, M.: Real-time stochastic optimization of complex energy systems on high-performance computers, Computing in Science & Engineering, 16, 32–42, 2014a.

10   Petra, C. G., Schenk, O., Lubin, M., and Gärtner, K.: An augmented incomplete factorization approach for computing the Schur complement in stochastic optimization, SIAM Journal on Scientific Computing, 36, C139–C162, 2014b.

Pirrung, G. R., Madsen, H. A., and Kim, T.: The influence of trailed vorticity on flutter speed estimations, Journal of Physics: Conference Series, 524, https://doi.org/10.1088/1742-6596/524/1/012048, 2014.

Rezaei, M., Zohoor, H., and Haddadpour, H.: Aeroelastic modeling and dynamic analysis of a wind turbine rotor by considering geometric
15   nonlinearities, Journal of Sound and Vibration, 432, 653–679, 2018.

Riziotis, V., Voutsinas, S., Politis, E., Chaviaropoulos, P., Hansen, A. M., Madsen, A., and Rasmussen, F.: Identification of structural non-linearities due to large deflections on a 5 MW wind turbine blade, Proceedings of the EWEC, 8, 2008.

Rubak, R. and Petersen, J. T.: Monopile as part of aeroelastic wind turbine simulation code, Proceedings of Copenhagen Offshore Wind, 2005.

20   Shabana, A. A.: Computational dynamics, John Wiley & Sons, 2010.

Shabana, A. A.: Dynamics of multibody systems, Cambridge university press, 2013.

Tibaldi, C., Henriksen, L. C., and Bak, C.: Investigation of the dependency of wind turbine loads on the simulation time, proceedings of EWEA 2014, 2014.

Verelst, D. R., Hansen, M. H., and Pirrung, G.: Steady State Comparisons HAWC2 v12. 2 vs HAWCStab2 v2. 12, Tech. Rep. Report-E-0122,
25   DTU Wind Energy, 2016.

Wang, Q., Sprague, M. A., Jonkman, J., Johnson, N., and Jonkman, B.: BeamDyn: a high-fidelity wind turbine blade solver in the FAST modular framework, Wind Energy, 2017.

Wilson, R. E. and Lissaman, P. B.: Applied aerodynamics of wind power machines, Tech. Rep. PB-238595, Oregon State University, USA, 1974.

30   Zierath, J., Rachholz, R., Woernle, C., and Müller, A.: Load calculation on wind turbines: validation of Flex5, Alaska/Wind, MSC. Adams and Simpack by means of field tests, ASME International Design Technical & Computers and Information in Engineering Conference, 2014.